Nanoscale

PAPER

View Article Online
View Journal | View Issue

Cite this: *Nanoscale*, 2016, **8**, 3008

Large area chemical vapor deposition of monolayer transition metal dichalcogenides and their temperature dependent Raman spectroscopy studies†

Amit S. Pawbake,[a,b] Mahendra S. Pawar,[a] Sandesh R. Jadkar[b] and Dattatray J. Late*[a]

Received 24th October 2015,
Accepted 5th January 2016

DOI: 10.1039/c5nr07401k

www.rsc.org/nanoscale

We investigate the growth mechanism and temperature dependent Raman spectroscopy of chemical vapor deposited large area monolayer of MoS_2, $MoSe_2$, WS_2 and WSe_2 nanosheets up to 70 μm in lateral size. Further, our temperature dependent Raman spectroscopy investigation shows that softening of Raman modes as temperature increases from 80 K to 593 K is due to the negative temperature coefficient and anharmonicity. The temperature dependent softening modes of chemical vapor deposited monolayers of all TMDCs were explained on the basis of a double resonance phonon process which is more active in an atomically thin sample. This process can also be fundamentally pertinent in other emerging two-dimensional layered and heterostructured materials.

Introduction

The atomically thin transition metal dichalcogenide (TMDC)[1–6] materials such as MoS_2, $MoSe_2$, WS_2, WSe_2, $MoTe_2$ *etc.* have been gaining much interest due to their prospective applications in nanoelectronic and optoelectronic devices.[1–8] For example, the bulk MoS_2 is semiconducting in nature and possesses an indirect band gap of 1.2 eV while the monolayer has a direct and wide band gap of 1.8 eV.[9] Similarly the monolayers of $MoSe_2$, WS_2, and WSe_2 possess a direct band gap of 1.58 eV,[10] 2.1 eV,[11] and 1.6 eV,[12] respectively. The tuning of the bandgap from a monolayer to bulk affects various properties such as electrical, optical, chemical, magnetic, and mechanical which indeed show its potential applications in various nanoelectronic and optoelectronic devices. Recently the chemical vapor deposition (CVD) method has been widely used to deposit nanosheets of various inorganic and other emerging materials due to fast, large area and controlled growth of materials.[13,14] The sample prepared under identical conditions by various research groups shows that the variation in the mobility is due to the poor quality of the sample.[15,16] It is important to understand the vibrational properties of these chalcogenide layered materials prepared under identical conditions and instruments.[17]

Raman spectroscopy is a very appropriate and advanced technique to characterize the structural, optical and mechanical properties of layered materials such as graphene,[18–24] MoS_2,[25–28] $MoSe_2$,[28–30] WS_2,[24,31,32] WSe_2,[28,29,33] $MoTe_2$,[34] WTe_2,[35] black phosphorus,[36] TiS_3 [37] and other layered materials.[38] The Raman spectroscopy technique is widely used to identify the number of layers present in graphene by monitoring the 2D bands position and intensity ratio, as well as used to find out the diameter of single walled carbon nanotubes (SWNTs)[39–43] and number of layers present in the 2D chalcogenide.[16–26] The investigations of the vibrational properties of chalcogenide layered materials are important to know the electron–phonon interaction, which plays a significant role in the electronic behavior of nanodevices and thus it can even affect the charge carrier mobility.[2,44] A systematic study of the vibrational properties of CVD grown MoS_2, WS_2, WSe_2 and $MoSe_2$ in a wide temperature range is still lacking in the literature. The Raman spectra of MoS_2 show a strong out-of-plane mode and in-plane mode as prominent peaks corresponding to the excitation of (E^1_{2g}) and (A_{1g}) Raman modes, whose frequencies exhibit a linear temperature dependence over the entire temperature range from 80 K to 593 K. The first order temperature coefficients (χ) associated with each Raman mode has been calculated from the slope of straight line fitted with a Raman shift as a function of temperature.[23,45] This observed variation with temperature in the Raman mode, is similar to that observed in other 2D systems including graphene.[46–48]

We present here the CVD grown monolayer MoS_2, $MoSe_2$, WS_2 and WSe_2 under an argon (Ar) atmosphere without using

[a]*Physical and Material Chemistry Division, CSIR – National Chemical Laboratory, Pune, 411008 Maharashtra, India. E-mail: datta099@gmail.com, dj.late@ncl.res.in*
[b]*School of Energy Studies, Department of Physics, Savitribai Phule Pune University, Pune 411007, India*

†Electronic supplementary information (ESI) available. See DOI: 10.1039/c5nr07401k

vacuum and present its temperature dependent Raman spectroscopy studies.

Experimental methods

Synthesis method

Chemical vapor deposition of single-layer MoS_2. We have synthesized monolayer MoS_2 by using the CVD method containing two heating zones (as shown in ESI Fig. S1(a)†). In a typical experiment, sulfur (S) powder (99.9%, Sigma Aldrich) was placed in the first zone at upstream, and molybdenum oxide (MoO_3) powder (99.5%, HPLC analytic reagent grade) was placed inside the quartz tube (50 mm dia.) in the second zone. Clean 300 nm SiO_2/Si wafers were then placed face down on the alumina boat which contains MoO_3 powder. The temperature of the second zone was raised up to 750 °C with a heating ramp of 10 °C min^{-1} and the deposition took place at 750 °C for 10 min. At the same time, the temperature of the first zone was also reached 120 °C so as to evaporate the sulfur powder. After the deposition, the furnace was allowed to cool naturally to room temperature. During the entire growth process, the argon flow rate was maintained at 50 SCCM.

Chemical vapor deposition of single-layer $MoSe_2$. In a typical experiment, selenium (Se) powder (99.9%, Sigma Aldrich) was placed in the first zone at upstream, and MoO_3 powder was placed inside the quartz tube (50 mm dia.) in the second zone. Clean 300 nm SiO_2/Si wafers were then placed face down on the alumina boat which contains MoO_3 powder. The temperature of the second zone was raised up to 750 °C with a heating ramp of 10 °C min^{-1} and deposition took place at 750 °C for 10 min. Further, the temperature of the first zone was also reached 250 °C so as to evaporate the Se powder at the same time of the reaction. After the reaction, the furnace was allowed to cool naturally to room temperature. During the entire growth process the flow rate of gas was maintained at 50 SCCM (Ar 40 SCCM + 10 SCCM H_2).

Chemical vapor deposition of single-layer WS_2. In a typical experiment, S powder was placed in the first zone of furnace at upstream and tungsten oxide (WO_3) powder (99.5%, HPLC analytic reagent grade) was placed inside the quartz tube (50 mm dia.) in the second zone. Clean 300 nm SiO_2/Si wafers were then placed face down on the alumina boat which contains WO_3 powder. The temperature of the second zone was raised up to 950 °C with a heating ramp of 10 °C min^{-1} and deposition took place at 950 °C for 10 min. Care has been taken for the temperature of the first zone to reach 120 °C at the same time of the reaction so as to evaporate the S powder. After the deposition the furnace was allowed to cool down naturally to room temperature. During the entire growth process, the Ar gas flow rate was maintained at 50 SCCM.

Chemical vapor deposition of single-layer WSe_2. In a typical experiment, Se powder was placed in the first zone at upstream and WO_3 powder was placed inside the quartz tube (50 mm dia.) in the second zone. Clean 300 nm SiO_2/Si wafers were then placed face down on the alumina boat which contains WO_3 powder. The temperature of the second zone was raised up to 950 °C with a heating ramp of 10 °C min^{-1} and the reaction were carried out at 950 °C for 10 min. The temperature of the first zone was raised to 250 °C so as to evaporate the Se powder at the same time of the reaction. After the deposition the furnace was allowed to cool down naturally to room temperature. During the entire growth process the gas flow rate was maintained at 50 SCCM (Ar 40 SCCM + 10 SCCM H_2).

Material characterization

Chemical vapor deposited monolayers of MoS_2, $MoSe_2$, WS_2, and WSe_2 were characterized using an optical microscope, atomic force microscopy (AFM) and Raman spectroscopy. The temperature dependent Raman spectroscopy of all TMDCs were carried out using a Renishaw InVia microscope Raman system with a laser wavelength of 532 nm in the back scattering geometry. The detector used was a CCD synapse with thermoelectric cooling to −70 °C. A 50× objective was used to focus the laser beam and to collect the Raman signal. The laser power on the sample was ~5 mW with a laser spot size ~1 μm to avoid the possible heating effect of the laser on the monolayer samples. The peak positions, intensity and line widths were determined by fitting the experimental data with Lorentzian functions. The optical images were captured using a Nikon Eclipse LV 150 NL optical microscope. Auto exposure times were used during the image recording, which can be varied in the range of 10–500 ms. The AFM images were acquired using a Bruker's multi code 8 instrument with tapping mode.

Results and discussion

Growth mechanism of single-layer TMDCs and morphology analysis

In the present investigations, we have synthesized monolayer TMDCs by a simple vapor solid mechanism using a tubular furnace. Fig. S2(a and b)† show the typical side view and top view of monolayer TMDCs. The formation of triangular shaped TMDC nanosheets and their growth mechanism completely depends on four factors: (i) gas flow rate, (ii) substrate temperature, (iii) a substrate which also plays an important role, and finally (iv) the ratio of M : X powder (where M = Mo, W and X = Se, S *etc.*). Fig. 1(a) shows a typical optical image of a triangular shaped single layer MoS_2 nanosheet with a typical lateral dimension of ~35 μm. The single-layer and few layer nature of MoS_2 and other TMDC samples was identified by using specific color contrast of layers with an optical microscope.[49,50] Further AFM images and AFM height profiles were analyzed so as to confirm the number of layers present in the sample. Additionally, the Raman spectrum was analyzed to identify the number of layers present in the MoS_2 nanosheet sample. Fig. 1(b) shows the typical Raman spectrum of a single layer MoS_2 recorded at room temperature. A typical Raman spectrum of a single-layer MoS_2 consisting of two modes E^1_{2g} and A_{1g} arises due to the in plane and out of plane modes. The in plane mode consists of vibration of two S atoms

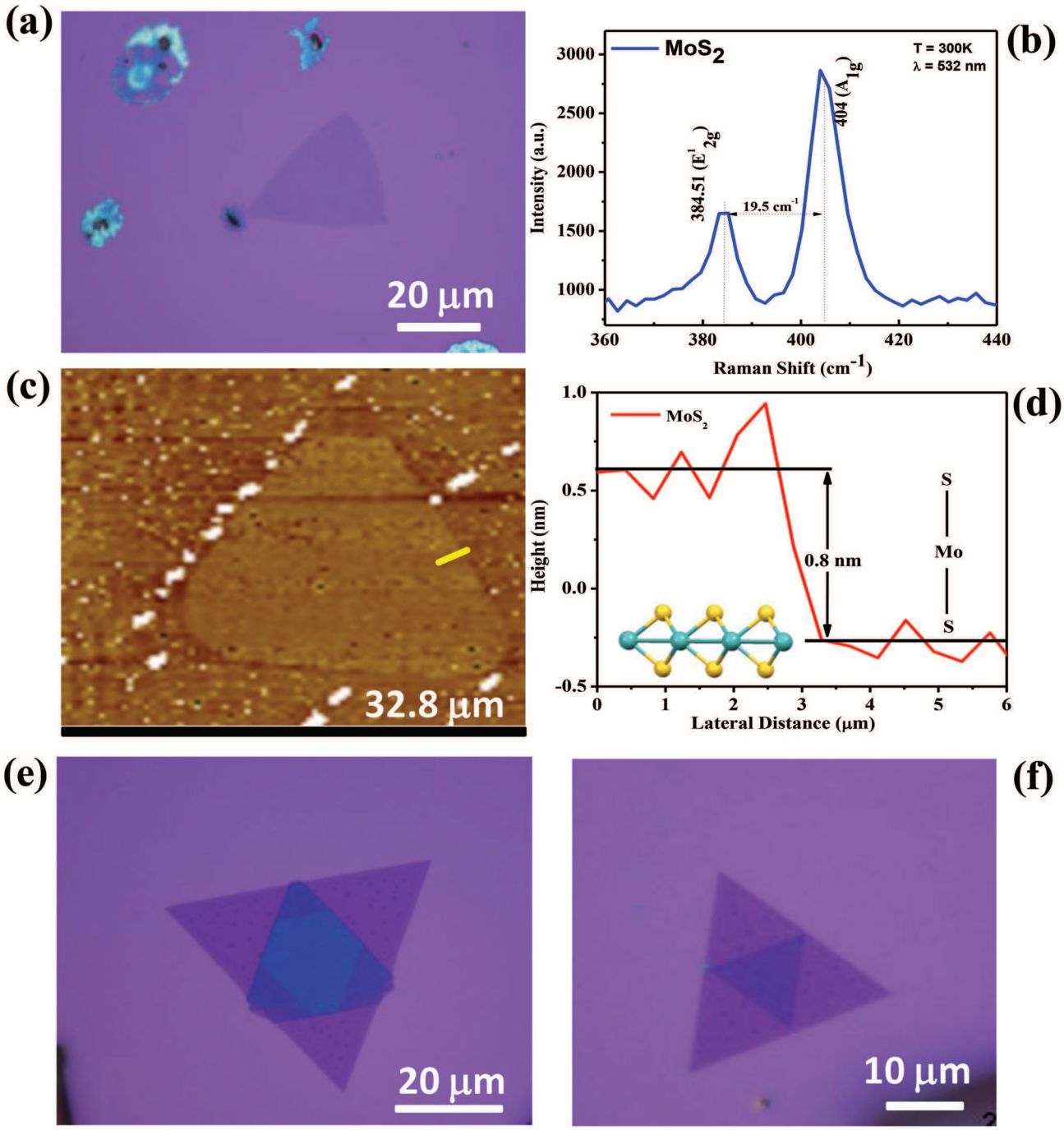

Fig. 1 Chemical vapor deposited single layer MoS_2 (a) typical optical image, (b) Raman spectrum, (c) AFM image, (d) corresponding AFM height profile and (e and f) optical images of stacked triangular shaped atomically thin MoS_2 layers grown at >750 °C.

in one direction and a Mo atom in the opposite direction. In the case of out of plane mode two S atoms vibrate opposite to each other while the Mo atom remains stable.[51] The peak frequency difference can also be monitored to find out the number of layers present in the sample. In the present case, the Raman frequency difference of E^1_{2g} and A_{1g} ~19.5 cm^{-1} was observed which indicates the single layer nature of MoS_2 nanosheet sample.[51,52] Fig. 1(c) shows a typical AFM image of a single-layer MoS_2 and Fig. 1(d) shows a typical AFM height profile which shows the thickness of nanosheets ~0.8 nm which confirms the single layer nature of MoS_2. Fig. 1(e and f) show typical optical images of MoS_2 synthesized at >750 °C which shows stacking of layers. Fig. 2(a) shows a typical optical image of a triangular shaped single layer $MoSe_2$ with a lateral dimension ~60 μm. Fig. 2(b) shows the typical Raman spectrum of a single layer $MoSe_2$ recorded at room temperature.

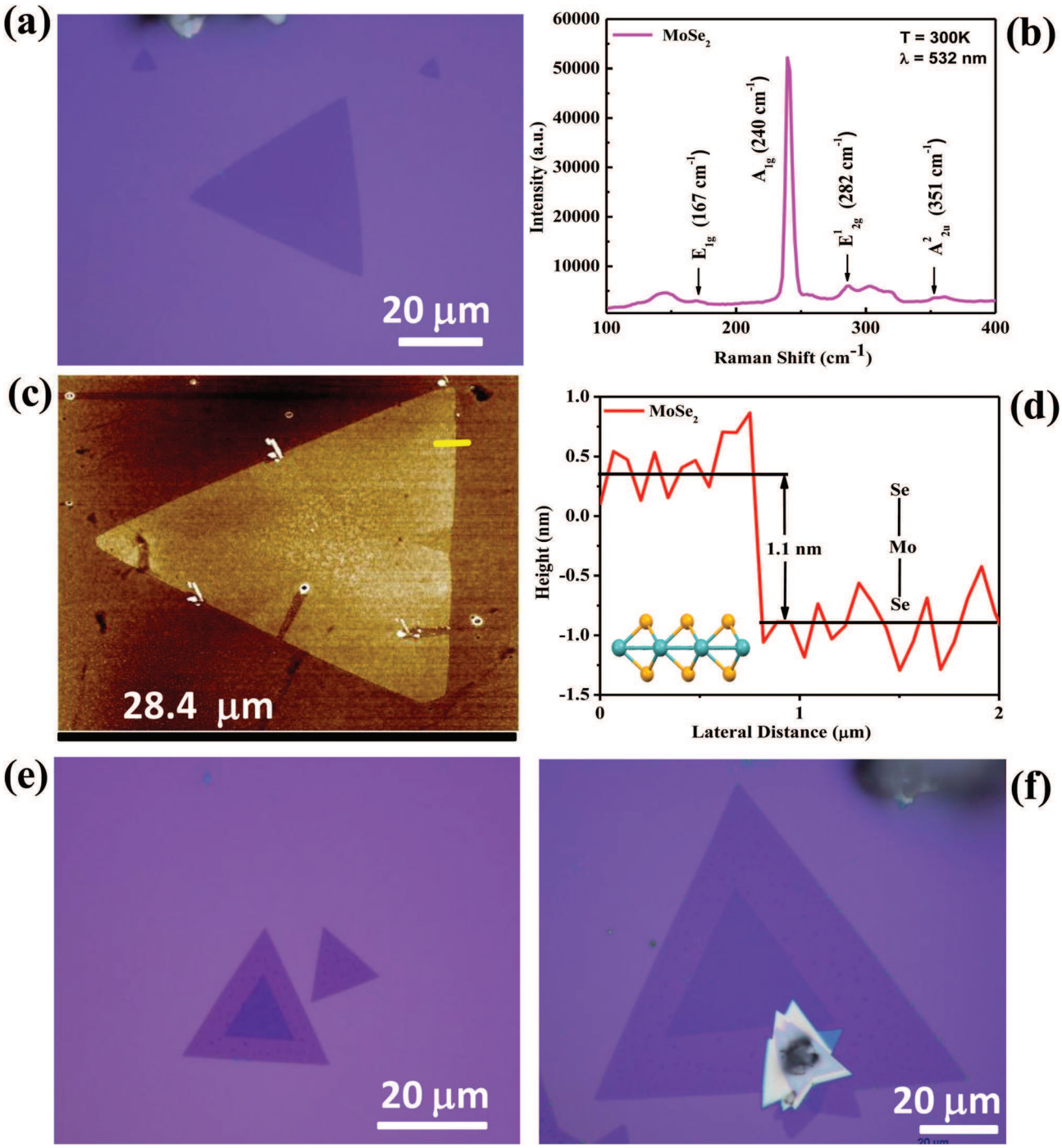

Fig. 2 Chemical vapor deposited single layer $MoSe_2$ (a) typical optical image, (b) Raman spectrum, (c) AFM image, (d) corresponding AFM height profile and (e and f) optical images of stacked triangular shaped atomically thin $MoSe_2$ nanosheets grown at >750 °C.

The most prominent peak A_{1g} is observed at 240 cm^{-1} due to out of plane vibration which undergoes softening of the A_{1g} mode in the monolayer due to decreasing inter-planar restoring force.[29,52] Fig. 2(c) shows a typical AFM image of a single-layer $MoSe_2$ nanosheet sample and Fig. 2(d) shows a typical AFM height profile with an observed thickness of the sample ~1.1 nm which confirms the single layer nature of the $MoSe_2$ nanosheet sample. Fig. 2(e and f) show typical optical images of $MoSe_2$ synthesized at >750 °C which show the stacking of layers. The evolution of interlayer coupling originates from the repulsive steric effects[53] that lead to different interlayer separations between the two MoS_2 layers in different stacking configurations as seen in the optical image of Fig. 1(e and f). According to the steric effect, each atom acquires a certain

amount of space that strongly repels each other due to a significant energy from the overlapping of electron clouds. The strong repulsion between two S atoms of the two different layers occurs when the S atom of the top layer sits on the S atom of the bottom layer in an eclipsed fashion at the interlayer distance. The atomic size and interlayer distance are the key parameters for observing the steric effect in layered materials.[53,54]

Fig. 3(a) shows a typical optical image of a single layer WS_2 with a lateral dimension of ~15 μm. Fig. 3(b) shows a typical Raman spectrum of a single layer WS_2 recorded at room temperature which consists of E^1_{2g} first order mode at 356.6 cm^{-1}, the Brillouin zone center and A_{1g} zone edge mode at 420 cm^{-1} which has been observed as a longitudinal acoustic mode *i.e.* LA (M) at the M point.[31,55] The LA (M) mode at 175 cm^{-1} arises

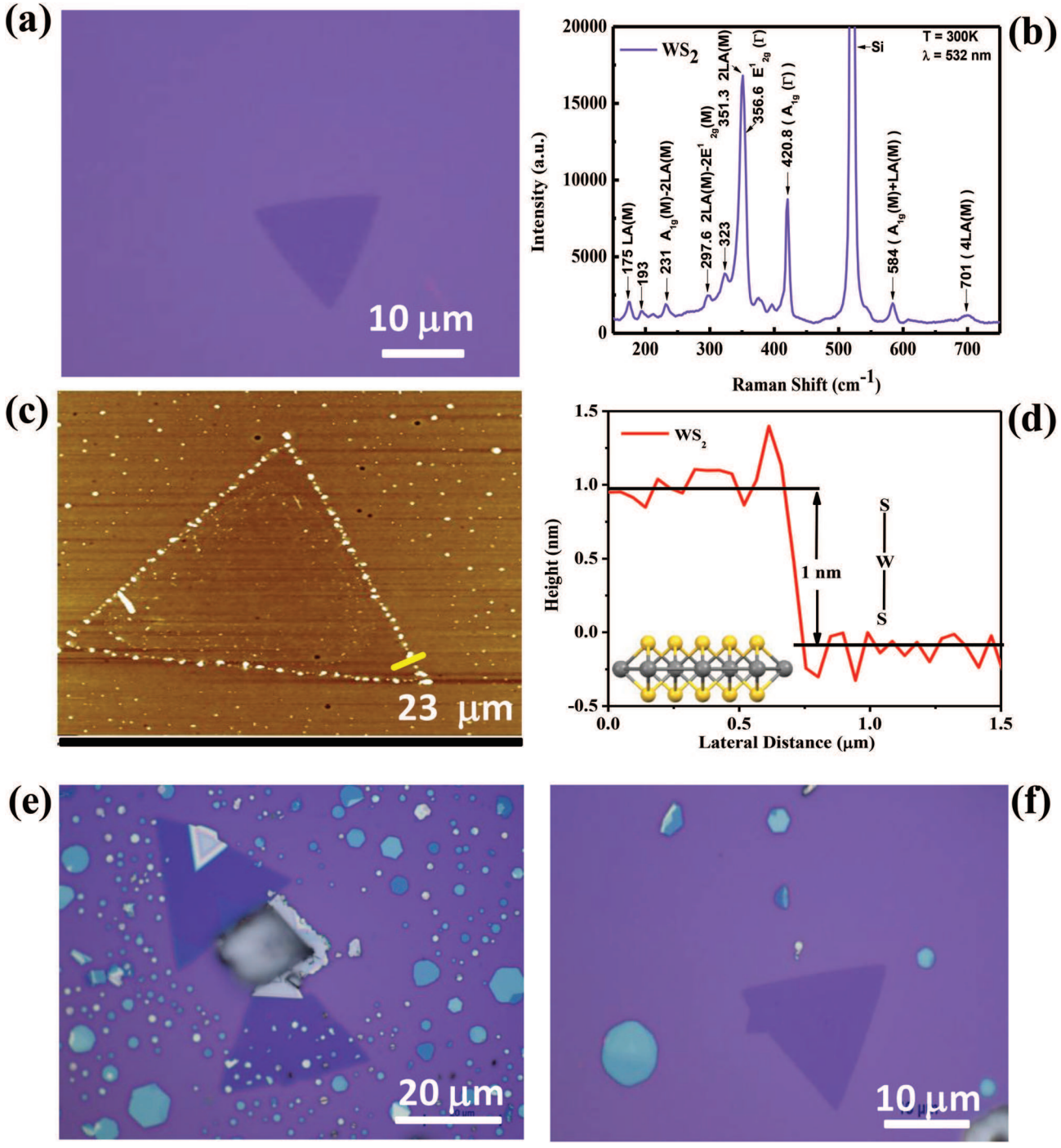

Fig. 3 Chemical vapor deposited single layer WS_2 (a) optical image, (b) Raman spectrum, (c) AFM image, (d) corresponding AFM height profile and (e and f) optical images of atomically thin hexagonal along with triangular shaped WS_2 nanosheets grown at >950 °C.

due to the M-point phonon which refers to the particular direction and magnitude q of the phonon.[31,55] The other peaks in the spectrum arise due to multi-phonon combinations of first order mode, zone edge mode and longitudinal acoustic mode.[31,56,57] It is well known that the intensity of the 2LA (M) peak increases with the decreasing number of layers and there is softening of A_{1g} mode due to the decreasing restoring force and fine stiffening of 2LA (M) and E^1_{2g} (Γ) modes accordant with the increasing restoring force which arises due to the van der Waals interactions between the layers.[57] Fig. 3(c) shows a typical AFM image of a single-layer WS_2 nanosheet sample and Fig. 3(d) shows the corresponding AFM height profile depicting the thickness of sample ~1 nm which confirms the single layer nature of a WS_2 nanosheet. Fig. 3(e and f) show typical

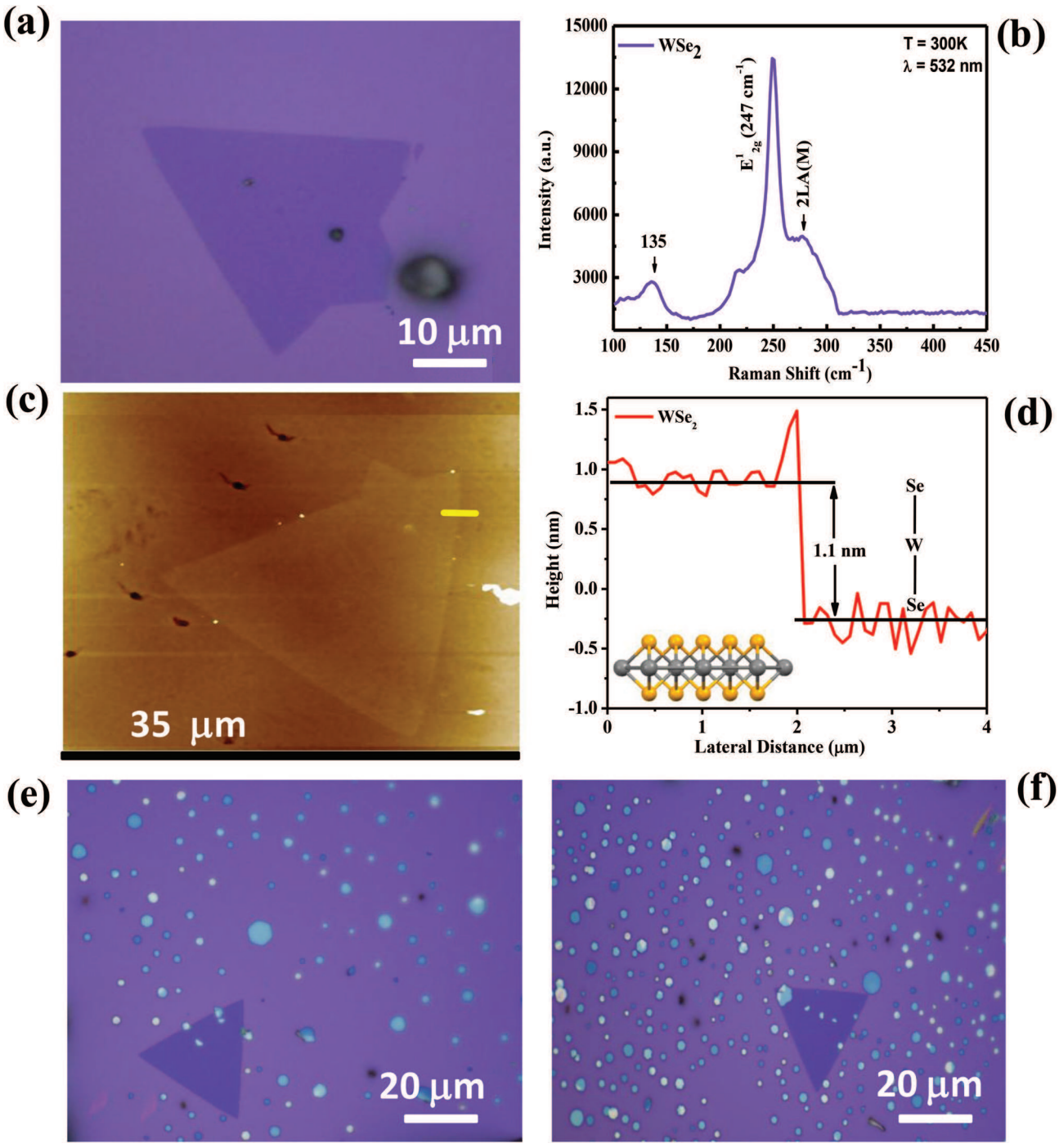

Fig. 4 Chemical vapor deposited single layer WSe_2 (a) typical optical image, (b) Raman spectrum, (c) AFM image, (d) corresponding AFM height profile and (e and f) optical images of atomically thin hexagonal along with triangle shaped WSe_2 nanosheets grown at >950 °C.

optical images of WS_2 nanosheets synthesized at >950 °C showing the few layer thick nature of a hexagonal shaped nanosheet sample along with monolayer triangles. Fig. 4(a) shows a typical optical image of a single layer WSe_2 with a lateral dimension of 30–60 μm. Fig. 4(b) shows the typical Raman spectrum of a single layer WSe_2 recorded at room temperature depicting the first order peak E^1_{2g} appearing at 247 cm^{-1} is due to the Brillouin zone center and zone edge phonons, the second order peak 2LA(M) observed is due to longitudinal acoustic phonons at the M-point in the Brillouin zone.[29,51,58,59] Fig. 4(c) shows a typical AFM image of single-layer WSe_2 nanosheets synthesized under an identical environment and Fig. 4(d) shows the corresponding AFM height profile with a thickness of 1.1 nm which indicates the single

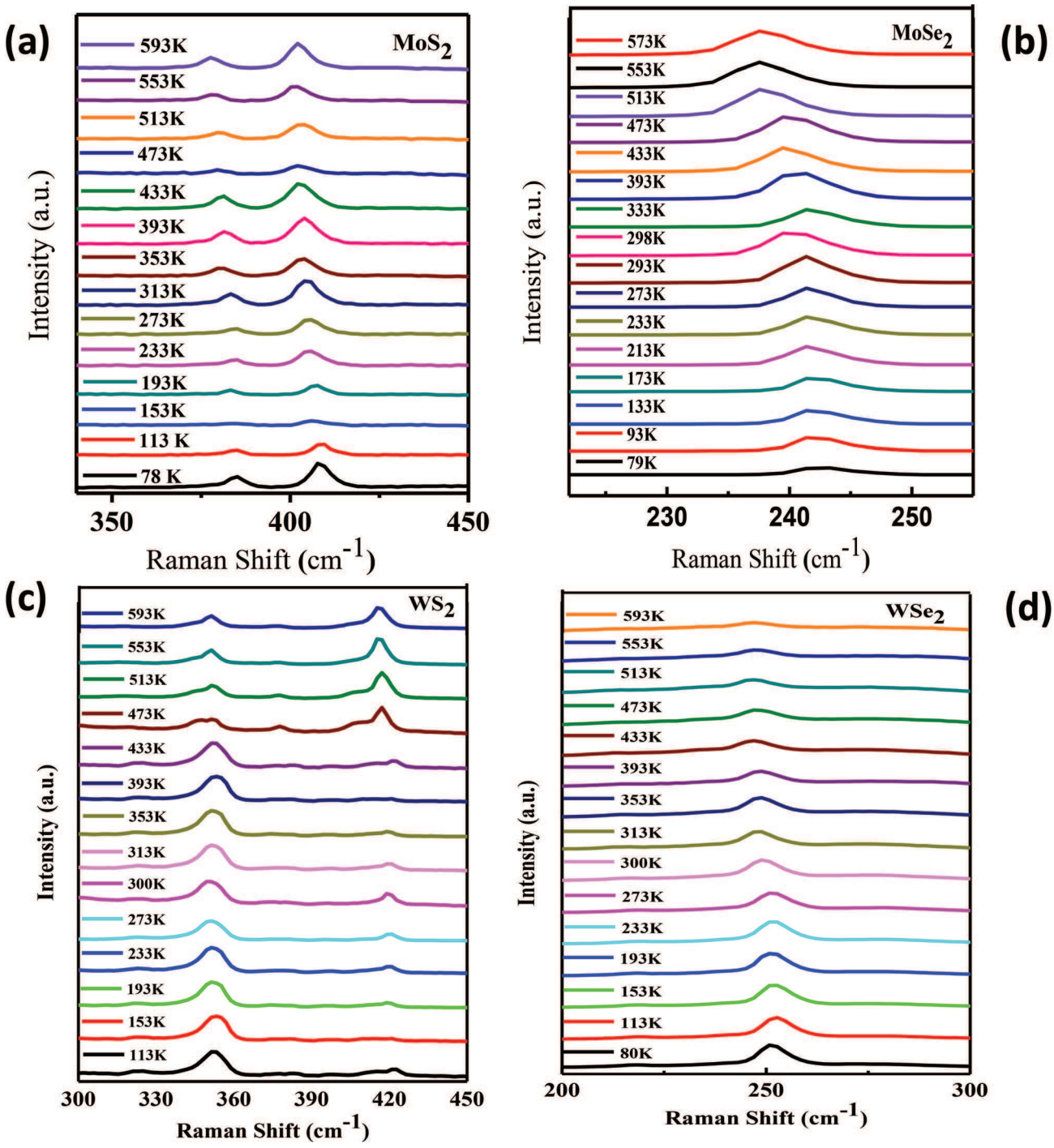

Fig. 5 Raman shift as a function of temperature for a chemical vapor deposited single layer (a) MoS_2, (b) $MoSe_2$, (c) WS_2 and (d) WSe_2.

layer nature of the WSe_2 nanosheet sample. Fig. 4(e and f) show typical optical images of WSe_2 nanosheets synthesized at >950 °C showing a few layer thick hexagonal shaped nanosheet sample along with monolayer triangles.

It is observed that if the growth temperature is >750 °C for the case of MoS_2 and $MoSe_2$ the monolayer along with bilayer sheets were also formed in 10 min of reaction time, which is shown in Fig. 1(e, f) and 2(e, f) respectively. At ~750 °C we

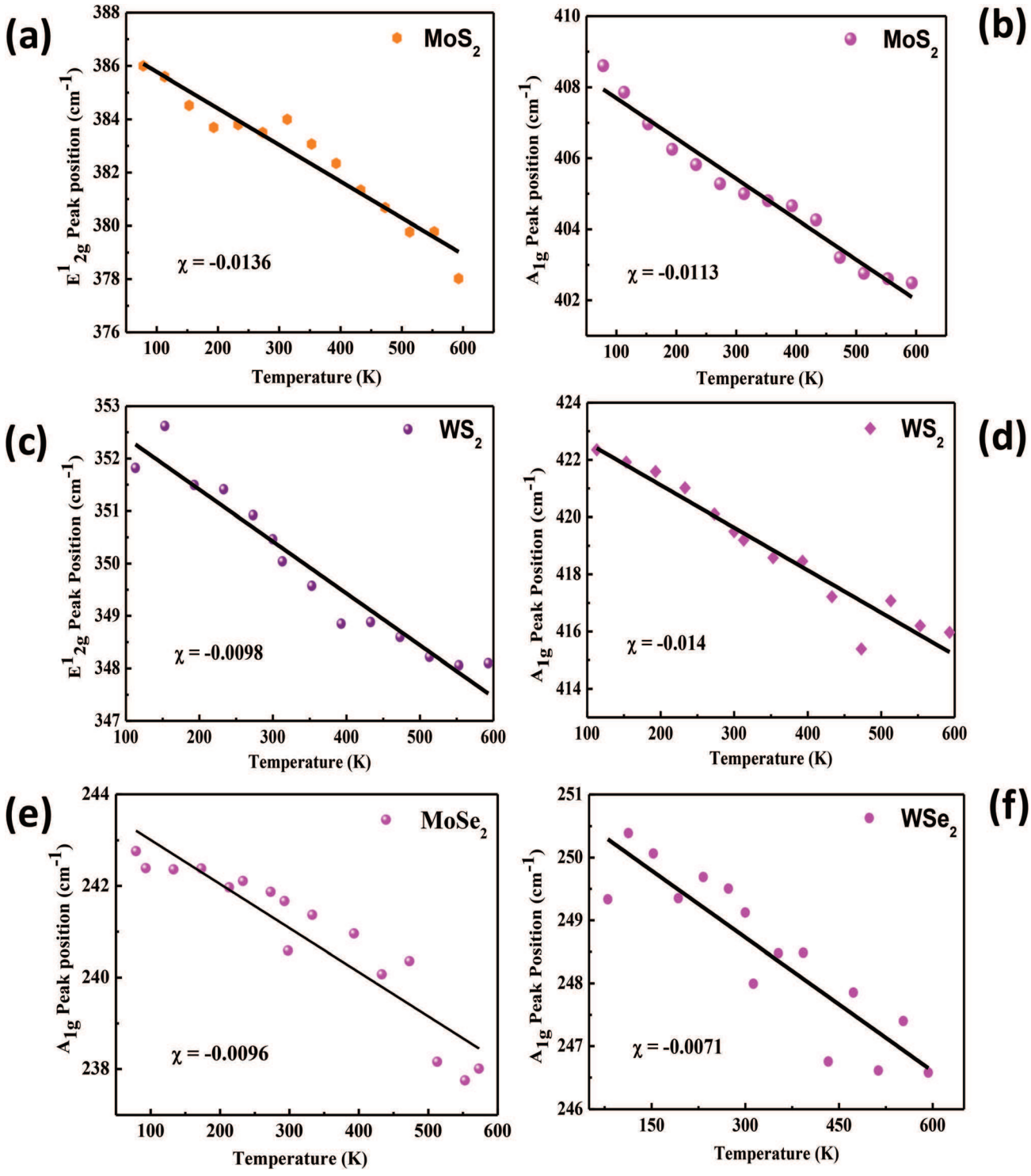

Fig. 6 Raman spectra peak position as a function of temperature for chemical vapor deposited monolayer MoS_2 with (a) E^1_{2g} and (b) A_{1g} mode, WS_2 (c) E^1_{2g} and (d) A_{1g} mode. For $MoSe_2$ (e) A_{1g} mode and for WSe_2 (f) A_{1g} mode respectively.

observed monolayers of MoS_2 and $MoSe_2$ which are shown in Fig. 1(a) and 2(a) respectively in 10 min of reaction time. In the case of WS_2 and WSe_2 we observed few layer hexagonal shapes along with monolayer triangles at >950 °C in 10 min of reaction time, which is shown in Fig. 3(e, f) and 4(e, f) respectively, while monolayer triangular shaped WS_2 and WSe_2 were observed for the reaction carried out at temperature (~950 °C) for 10 min as seen from the optical images shown in Fig. 3(a) and 4(a). Bilu Liu *et al.*[60] reported that in the case of monolayer WSe_2 shape evolution completely depends on the substrate temperature. It is also observed that lateral sizes of the triangles are more on insulating substrates such as SiO_2 and quartz as compared to the conducting substrates such as p-Si and n-Si (see ESI Fig. S3† for optical images). Shanshan Wang *et al.*[61] reported that, if the Mo : S ratio is >1 : 2 then it forms a triangular shaped nanosheet with Mo as the terminate boundary. The majority of monolayer samples are well aligned with the relative orientation of edges that can be termed as multiples of 60° which can be confirmed by measuring the area of an equilateral triangle.[61] If the Mo : S ratio is equal to 1 : 2 then a hexagonal shaped monolayer with Mo and S terminate boundary were formed. If the Mo : S ratio is less than 1 : 2 then triangular shaped TMDC monolayers were formed.[61]

Temperature dependent Raman spectroscopy of TMDCs

Fig. S1(b)† shows a typical experimental set-up used to carry out the temperature dependent Raman spectroscopy studies of monolayer TMDCs. Fig. 5(a) and (b) represent typical Raman shift *versus* temperature plots for the CVD grown monolayer MoS_2 and $MoSe_2$ nanosheet samples respectively. From the plot it is clearly seen that there is downward shift in the Raman modes with increasing temperature. Further, with increasing temperature an increase in the full width at half maximum (FWHM) of the peak was observed for all the monolayer TMDCs. Fig. 5(c) and (d) show the typical plot for the Raman shift as a function of temperature for the CVD grown WS_2 and WSe_2 nanosheet samples respectively. The plot clearly shows the downward shift in the Raman modes with increasing temperature. Apparently, the temperature dependence of the Raman spectra of all these chalcogenide nanosheets is similar to graphene.[46,48] Fig. 6(a–f) show the typical plots for Raman spectra peak positions as a function of temperature for the monolayer MoS_2, WS_2, $MoSe_2$, and WSe_2 samples respectively. The possible vibrational modes of TMDCs are shown in ESI Fig. S4.† The Raman modes for MoS_2, WS_2, $MoSe_2$, and WSe_2 behave linearly with the temperature range from 80 K to 593 K. The Raman peak positions were calculated by fitting the Lorentzian functions for each mode as a function of temperature given by eqn (1),[62]

$$\omega(T) = \omega_0 + \chi T \quad (1)$$

where ω_0 is the peak position of A_{1g}, $E^1{}_{2g}$ and B_{2g} vibration modes at zero Kelvin temperature, and χ is the first order temperature coefficient of the A_{1g}, $E^1{}_{2g}$ and B_{2g} modes. The Raman modes A_{1g}, $E^1{}_{2g}$ and B_{2g} behave linearly with temperature and the slope of the fitted straight line gives the temperature coefficient (χ). The calculated values of temperature coefficients and change in Raman frequency as a function of temperature for different modes are shown in Table 1. The change in the Raman modes with the temperature is mostly due to the contribution from the thermal anharmonicity *i.e.* from thermal expansion and volume contribution. The Raman phonon frequency ω as a function of temperature and volume is shown below,[63]

Table 1 The temperature coefficients and frequency difference for chemical vapor deposited single-layer TMDCs

Monolayer TMDCs	Raman modes	Observed temp. coefficient χ (cm^{-1} K^{-1})	$\Delta\omega$ (cm^{-1})
MoS_2	$E^1{}_{2g}$	−0.0136	8
	A_{1g}	−0.0113	6.11
$MoSe_2$	A_{1g}	−0.0096	4.75
WS_2	$E^1{}_{2g}$	−0.0098	4.51
	A_{1g}	−0.014	6.43
WSe_2	A_{1g}	−0.0071	3.81

$$\left(\frac{\partial \ln \omega}{\partial T}\right)P = \left(\frac{\partial \ln V}{\partial T}\right)P\left(\frac{\partial \ln \omega}{\partial \ln V}\right)T + \left(\frac{\partial \ln \omega}{\partial T}\right)V$$
$$\left(\frac{\partial \ln \omega}{\partial T}\right)P = -\frac{\gamma}{k}\left(\frac{\partial \ln \omega}{\partial P}\right)T + \left(\frac{\partial \ln \omega}{\partial T}\right)V \quad (2)$$

where $\gamma \approx (\partial \ln V/\partial T)P$ and $k \approx -(\partial \ln V/\partial P)T$ are the volume thermal coefficient and isothermal volume compressibility respectively. The first term on the right hand side of eqn (2) gives the volume contribution at a constant temperature and the second term represents the temperature contribution at a constant volume. The anharmonic contribution can be calculated from the values of isobaric temperature, and the isothermal pressure derivative of phonon frequencies of the modes, Υ, κ. The change in FWHM, intensity and shift in the peak position as a function of temperature can be explained by using the double resonance phenomenon which is very active in single layer samples. The broadening in the Raman modes with temperature is based on phonon dispersion and many-body theoretical calculations. The change in FWHM is mainly due to the contribution from the decay of a zone center optical phonon into one acoustic and one optical phonon and these two phonons were selected from the phonon density states of all the TMDCs. The change in line width as a function of temperature is given by the equation,[64]

$$\Gamma(T) = \Gamma_0 + A[1 + n(\omega_1, T) + n(\omega_2, T)] \quad (3)$$

where Γ_0 represents the background contribution, A is the anharmonic coefficient and $n(\omega,T)$ is the Bose–Einstein contribution function. The temperature dependent FWHM can be determined from the parameters such as Γ_0, A, ω_1 and ω_2. The change in Raman frequency ($\Delta\omega$) for the Raman modes $E^1{}_{2g}$, and A_{1g}, in monolayer MoS_2 was found to be 8 and 6.11 cm^{-1} respectively, for A_{1g} in $MoSe_2$ it was 4.75, in the case of WS_2 for $E^1{}_{2g}$ and A_{1g} the calculated values were 4.51 and 6.43 cm^{-1}

respectively. The change in Raman frequency of the Raman modes A_{1g} in monolayer WSe_2 was found to be 3.81 cm^{-1}.

Conclusion

In conclusion, we have systematically reported the CVD growth of large area single layer MoS_2, $MoSe_2$, WS_2 and WSe_2 and studied its temperature dependent Raman spectroscopy. We have extracted the values of temperature coefficient and observed the change in Raman peak positions with varying temperature for monolayer TMDCs. The shifts in the Raman spectra of TMDCs were mainly contributed from the thermal and anharmonic properties. The softening of all the Raman modes was further explained in terms of the double resonance phenomenon which is very active in single layer samples. The temperature dependent Raman spectroscopy method can also be applicable in monitoring the device performance and other emerging properties of various other layered materials.

Acknowledgements

Dr D. J. Late would like to thank Prof. C. N. R. Rao (FRS), JNCASR and ICMS Bangalore (India) for encouragement and support. The research work was supported by the Department of Science and Technology (Government of India) under a Ramanujan Fellowship to Dr D. J. Late (Grant No. SR/S2/RJN-130/2012), NCL-MLP project grant 028626, DST-SERB Fast-track Young scientist project Grant No. SB/FT/CS-116/2013, Broad of Research in Nuclear Sciences (BRNS Grant No. 34/14/20/2015 (Government of India), partial support by INUP IITB project sponsored by DeitY, MCIT, Government of India. Authors would like to thank Director, CSIR-National Chemical Laboratory for the experimental facilities.

Notes and references

1 K. S. Novoselov, D. Jiang, F. Schedin, T. J. Booth, V. V. Khotkevich, S. V. Morozov and A. K. Geim, *Proc. Natl. Acad. Sci. U. S. A.*, 2005, **102**, 10451–10453.
2 Q. H. Wang, K. Kolantar-Zadeh, A. Kis, J. N. Coleman and M. S. Strano, *Nat. Nanotechnol.*, 2012, **7**, 699–712.
3 B. Liu, M. Kopf, A. A. Abbas, X. Wang, Q. Guo, Y. Jia, F. Xia, R. Weihrich, F. Bachhuber, F. Pielnhofer, H. Wang, R. Dhall, S. B. Cronin, M. Ge, X. Fang, T. Nilges and C. Zhou, *Adv. Mater.*, 2015, **27**, 4423–4429.
4 B. Liu, L. Chen, G. Liu, A. N. Abbas, M. Fathi and C. Zhou, *ACS Nano*, 2014, **8**, 5304–5314.
5 L. Chen, B. Liu, A. N. Abbas, Y. Ma, X. Fang, Y. Liu and C. Zhou, *ACS Nano*, 2014, **8**, 11543–11551.
6 L. Chen, B. Liu, M. Ge, Y. Ma, A. N. Abbas and C. Zhou, *ACS Nano*, 2015, **9**, 8368–8375.
7 D. J. Late, B. Liu, H. R. Matte, V. P. Dravid and C. N. R. Rao, *ACS Nano*, 2012, **6**, 5635–5641.
8 D. J. Late, Y. K. Huang, B. Liu, J. Acharya, S. N. Shirodkar, J. Luo, A. Yan, D. Charles, U. V. Waghmare, V. P. Dravid and C. N. R. Rao, *ACS Nano*, 2013, **7**, 4879–4891.
9 K. F. Mak, C. Lee, J. Hone, J. Shan and T. F. Heinz, *Phys. Rev. Lett.*, 2010, **105**, 136805.
10 Y. Zhang, T.-R. Chang, B. Zhou, Y.-T. Cui, H. Yan, Z. Liu, F. Schmitt, J. Lee, R. Moore, Y. Chen, H. Lin, H.-T. Jeng, S.-K. Mo, Z. Hussain, A. Bansil and Z.-X. Shen, *Nat. Nanotechnol.*, 2014, **9**, 111–115.
11 T. Georgiou, R. Jalil, B. D. Belle, L. Britnell, R. V. Gorbachev, S. V. Morozov, Y.-J. Kim, A. Gholinia, S. J. Haigh, O. Makarovsky, L. Eaves, L. A. Ponomarenko, A. K. Geim, K. S. Novoselov and A. Mishchenko, *Nat. Nanotechnol.*, 2013, **8**, 100–103.
12 W. Liu, J. Kang, D. Sarkar, Y. Khatami, D. Jena and K. Banerjee, *Nano Lett.*, 2013, **13**, 1983–1990.
13 G. He, K. Ghosh, U. Singisetti, H. Ramamoorthy, R. Somphonsane, G. Bohra, M. Matsunaga, A. Higuchi, N. Aoki, S. Najmaei, Y. Gong, X. Zhang, R. Vajtai, P. M. Ajayan and J. P. Bird, *Nano Lett.*, 2015, **15**, 5052–5058.
14 Y. Ma, B. Liu, A. Zhang, L. Chen, M. Fathi, C. Shen, A. N. Abbas, M. Ge, M. Mecklenburg and C. Zhou, *ACS Nano*, 2015, **9**, 7383–7391.
15 Y. Zhang, Y. Zhang, Q. Ji, J. Ju, H. Yuan, J. Shi, T. Gao, D. Ma, M. Liu, Y. Chen, X. Song, H. Y. Hwang, Y. Cui and Z. Liu, *ACS Nano*, 2013, **7**, 8963–8971.
16 Y.-H. Lee, L. Yu, H. Wang, W. Fang, X. Ling, Y. Shi, C.-T. Lin, J.-K. Huang, M.-T. Chang, C.-S. Chang, M. Dresselhaus, T. Palacios, L.-J. Li and J. Kong, *Nano Lett.*, 2013, **13**, 1852–1857.
17 Q. Ji, Y. Zhang, Y. Zhang and Z. Liu, *Chem. Soc. Rev.*, 2015, **44**, 2587–2602.
18 N. Bonini, M. Lazzeri, N. Marzari and F. Mauri, *Phys. Rev. Lett.*, 2007, **99**, 176802–176805.
19 A. C. Ferrari, J. C. Meyer, V. Scardaci, C. Casiraghi, M. Lazzeri, F. Mauri, D. Piscanec, S. Jiang, K. S. Novoselov, S. Roth and A. K. Geim, *Phys. Rev. Lett.*, 2006, **97**, 187401–107404.
20 L. M. Malard, M. A. Pimenta, G. Dresselhaus and M. S. Dresselhaus, *Phys. Rep.*, 2009, **473**, 51–87.
21 I. Calizo, F. Miao, W. Bao, C. N. Lau and A. A. Balandin, *Appl. Phys. Lett.*, 2007, **91**, 071913–071915.
22 A. Gupta, G. Chen, P. Joshi, S. Tadigadapa and P. C. Eklund, *Nano Lett.*, 2006, **6**, 2667–2673.
23 I. Calizo, A. A. Balandin, W. Bao, F. Miao and C. N. Lau, *Nano Lett.*, 2007, **7**, 2645–2649.
24 R. Narula and S. Reich, *Phys. Rev. B: Condens. Matter*, 2008, **78**, 165422–165427.
25 Y. Wang, C. Cong, C. Qiu and T. Yu, *Small*, 2013, **9**, 2857–2861.
26 R. Yan, J. R. Simpson, S. Bertolazzi, J. Brivio, M. Watson, X. Wu, A. Kis, T. Luo, A. R. H. Walker and H. G. Xing, *ACS Nano*, 2014, **8**, 986–993.
27 M. Thripuranthaka, R. V. Kashid, C. S. Rout and D. J. Late, *Appl. Phys. Lett.*, 2014, **104**, 081911–081915.

28 P. Tanndorf, R. Schmidt, P. Bottger, X. Zhang, J. Borner, A. Lietrig, M. Albretch, C. Kloc, O. Gordan, D. R. T. Zahn, S. M. de Vasconcellos and R. Bratschitsch, *Opt. Express*, 2013, **21**, 4908–4916.
29 D. J. Late, S. N. Shirodkar, U. V. Waghmare, V. P. Dravid and C. N. R. Rao, *ChemPhysChem*, 2014, **15**, 1592–1598.
30 D. J. Late, T. Doneux and M. Bougouma, *Appl. Phys. Lett.*, 2014, **105**, 233103.
31 A. Berkdemir, H. R. Gutierrez, A. R. Bontello-Mendez, N. Perea-Lopez, A. L. Elias, C.-I. Chia, B. Wang, V. H. Crespi, F. Lopez-Urias, J.-C. Charlier, H. Terrones and M. Terrones, *Sci. Rep.*, 2013, **3**, 1755–1762.
32 M. Thripuranthaka and D. J. Late, *ACS Appl. Mater. Interfaces*, 2014, **6**, 1158–1163.
33 X. Luo, Y. Zhao, M. Toh, C. Kloc, Q. Xiong and S. Y. Quek, *Phys. Rev. B: Condens. Matter*, 2013, **88**, 195313–195319.
34 M. Yamamoto, S. T. Wang, M. Ni, Y. F. Lin, S. L. Li, S. Aikawa, W. B. Jian, K. Ueno, K. Wakabayashi and K. Tsukagoshi, *ACS Nano*, 2014, **8**, 3895–3903.
35 M. K. Jana, A. Singh, D. J. Late, C. Rajamathi, K. Biswas, C. Felser, U. V. Waghmare and C. N. R. Rao, *J. Phys.: Condens. Matter*, 2015, **27**, 285401.
36 M. Buscema, D. J. Groenendijk, S. I. Blanter, G. A. Steele, H. S. J. van der Zant and A. Castellanos-Gomez, *Nano Lett.*, 2014, **14**, 3347–3352.
37 A. S. Pawbake, J. O. Island, E. Flores, J. R. Ares, C. Sanchez, I. J. Ferrer, S. R. Jadkar, H. S. vander Zant, A. Castellanos-Gomez and D. J. Late, *ACS Appl. Mater. Interfaces*, 2015, **7**, 24185–24190.
38 D. J. Late, B. Liu, J. Luo, A. Yan, H. S. S. R. Matte, M. Grayson, C. N. R. Rao and V. P. Dravid, *Adv. Mater.*, 2012, **24**, 3549–3554.
39 P. V. Huong, R. Cavagnat, P. M. Ajayan and O. Stephan, *Phys. Rev. B: Condens. Matter*, 1995, **51**, 10048–10051.
40 L. Song, W. Ma, Y. Ren, W. Zhou, S. Xie, P. Tan and L. Sun, *Appl. Phys. Lett.*, 2008, **92**, 121905–121908.
41 Y. Wang, D. C. Alsmeyer and R. L. McCreery, *Chem. Mater.*, 1990, **2**, 557–563.
42 R. Saito, A. Gruneis, G. G. Samsonidze, V. W. Brar, G. Dresselhaus, M. S. Dresselhaus, A. Jorio, L. G. Cancado, C. Fantini, M. A. Pimenta and A. G. S. Filho, *New J. Phys.*, 2003, **5**, 157–171.
43 M. Souza, A. Jorio, C. Fantini, B. R. A. Neves, M. A. Pimenta, R. Saito, A. Ismach, E. Joselevich, V. W. Brar, G. G. Samsonidze, G. Dresselhaus and M. S. Dresselhaus, *Phys. Rev. B: Condens. Matter*, 2004, **69**, 241403–241406.
44 D. Lembke, S. Bertolazzi and A. Kis, *Acc. Chem. Res.*, 2015, **48**, 100–110.
45 N. R. Raravikar, P. Keblinski, A. M. Rao, M. S. Dresselhaus, L. S. Schadler and P. M. Ajayan, *Phys. Rev. B: Condens. Matter*, 2002, **66**, 235424.
46 D. J. Late, U. Maitra, L. S. Panchakarla, U. V. Waghmare and C. N. R. Rao, *J. Phys.: Condens. Matter*, 2011, **23**, 055303.
47 K. V. Zakharchenko, M. I. Katsnelson and A. Fasolino, *Phys. Rev. Lett.*, 2009, **102**, 046808.
48 A. Taube, J. Judek, C. Jastrzebski, A. Duzynska, K. Switkowski and M. Zdrojek, *ACS Appl. Mater. Interfaces*, 2014, **6**, 8959–8963.
49 D. J. Late, B. Liu, H. S. S. Matte, C. N. R. Rao and V. P. Dravid, *Adv. Funct. Mater.*, 2012, **22**, 1894–1905.
50 A. C. Gomez, N. Agraït and G. R. Bollinger, *Appl. Phys. Lett.*, 2010, **96**, 213116.
51 H. Li, Q. Zhang, C. C. R. Yap, B. K. Tay, T. H. T. Edwin, A. Olivier and D. Baillargeat, *Adv. Funct. Mater.*, 2012, **22**, 1385–1390.
52 C. Lee, H. Yan, L. E. Brus, T. F. Heinz, J. Hone and S. Ryu, *ACS Nano*, 2010, **4**, 2695–2700.
53 K. Liu, L. Zhang, T. Cao, C. Jin, D. Qiu, Q. Zhou, A. Zettl, P. Yang, S. G. Louie and F. Wang, *Nat. Commun.*, 2014, **5**, 4966.
54 G. C. Constantinescu and N. D. Hine, *Phys. Rev. B: Condens. Matter*, 2015, **91**, 195416.
55 M. Staiger, R. Gillen, N. Scheuschner, O. Ochedowski, F. Kampmann, M. Schleberger, C. Thomsen and J. Maultzsch, *Phys. Rev. B: Condens. Matter*, 2015, **91**, 195419.
56 A. R. Beal and W. Y. Liang, *J. Phys. C: Solid State Phys.*, 1976, **9**, 2459–2466.
57 C. Sourisseau, F. Cruege and M. Fouassier, *Chem. Phys.*, 1991, **150**, 281–293.
58 A. Molina-Sanchez and L. Wirtz, *Phys. Rev. B: Condens. Matter*, 2011, **84**, 155413–155421.
59 E. D. Corro, H. Terrones, A. Elias, C. Fantini, S. Feng, M. A. Nguyen, T. E. Mallouk, M. Terrones and M. A. Pimenta, *ACS Nano*, 2014, **8**, 9629–9635.
60 B. Liu, M. Fathi, L. Chen, A. Abbas, Y. Ma and C. Zhou, *ACS Nano*, 2015, **9**, 6119–6127.
61 S. Wang, Y. Rong, Y. Fan, M. Pacios, H. Bhaskaran, K. He and J. H. Warner, *Chem. Mater.*, 2014, **26**, 6371–6379.
62 D. J. Late, *ACS Appl. Mater. Interfaces*, 2015, **7**, 5857–5862.
63 P. S. Peercy and B. Morosin, *Phys. Rev. B: Solid State*, 1973, **7**, 2779–2786.
64 J. Menendez and M. Cardona, *Phys. Rev. B: Condens. Matter*, 1984, **29**, 2051.

Nanoscale

ARTICLE

Electronic Supplementary Material

Large area chemical vapor deposition of monolayer transition metal dichalcogenides and their Temperature Dependent Raman Spectroscopy studies

*Amit S. Pawbake, [a,b] Mahendra S. Pawar,[b] Sandesh R. Jadkar, [a] Dattatray J. Late [b]**

[a,]Physical and Material Chemistry Division, CSIR – National Chemical Laboratory, Pune, 411008, Maharashtra, India. E-mail: datta099@gmail.com; dj.late@ncl.res.in*

[b]School of Energy Studies, Department of Physics, Savitribai Phule Pune University, Pune 411007, India.

Figure S1:

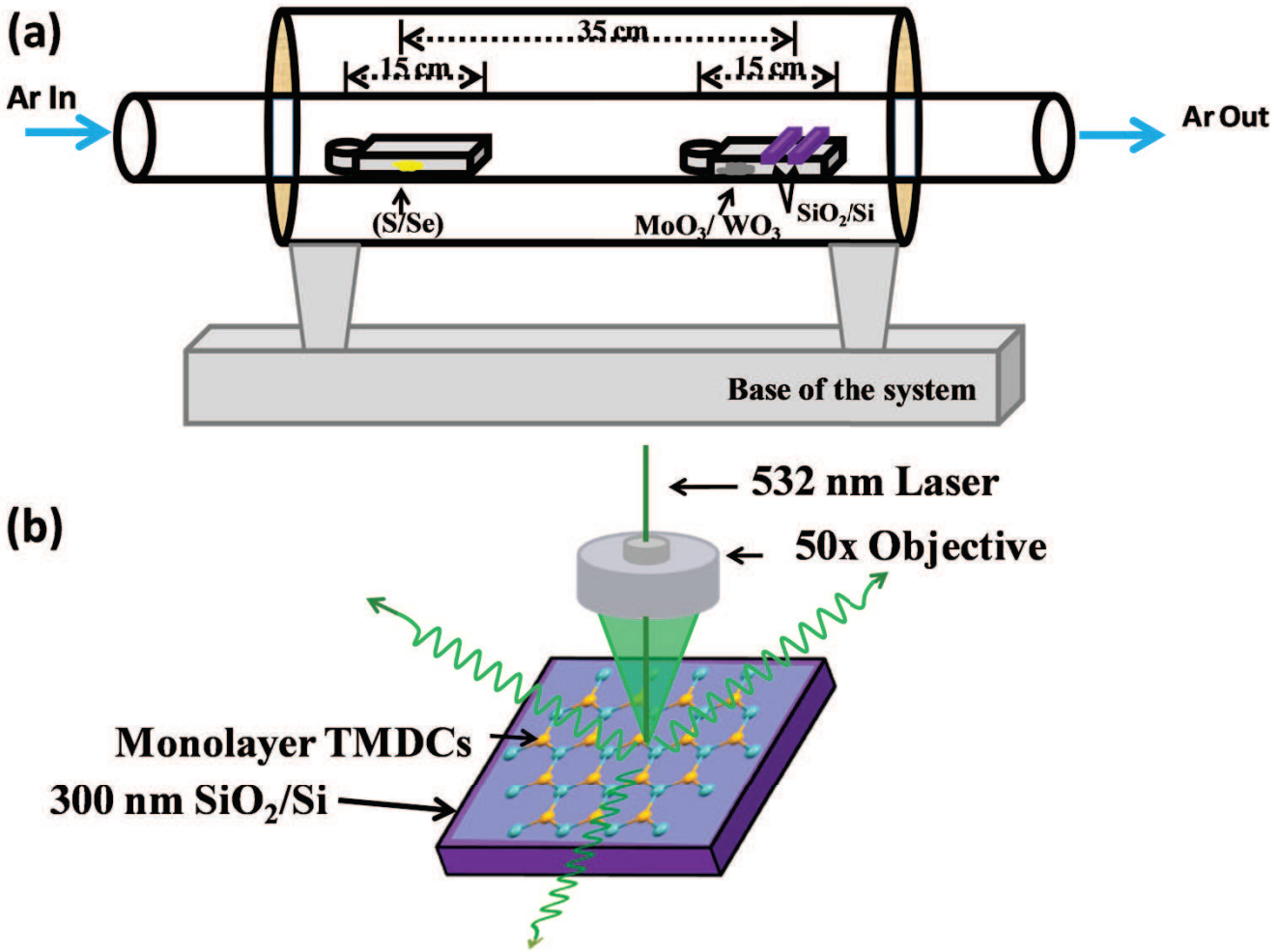

Figure S1: Experimental set up of (a) chemical vapor deposition and (b) Temperature dependant Raman Spectroscopy.

Figure S2:

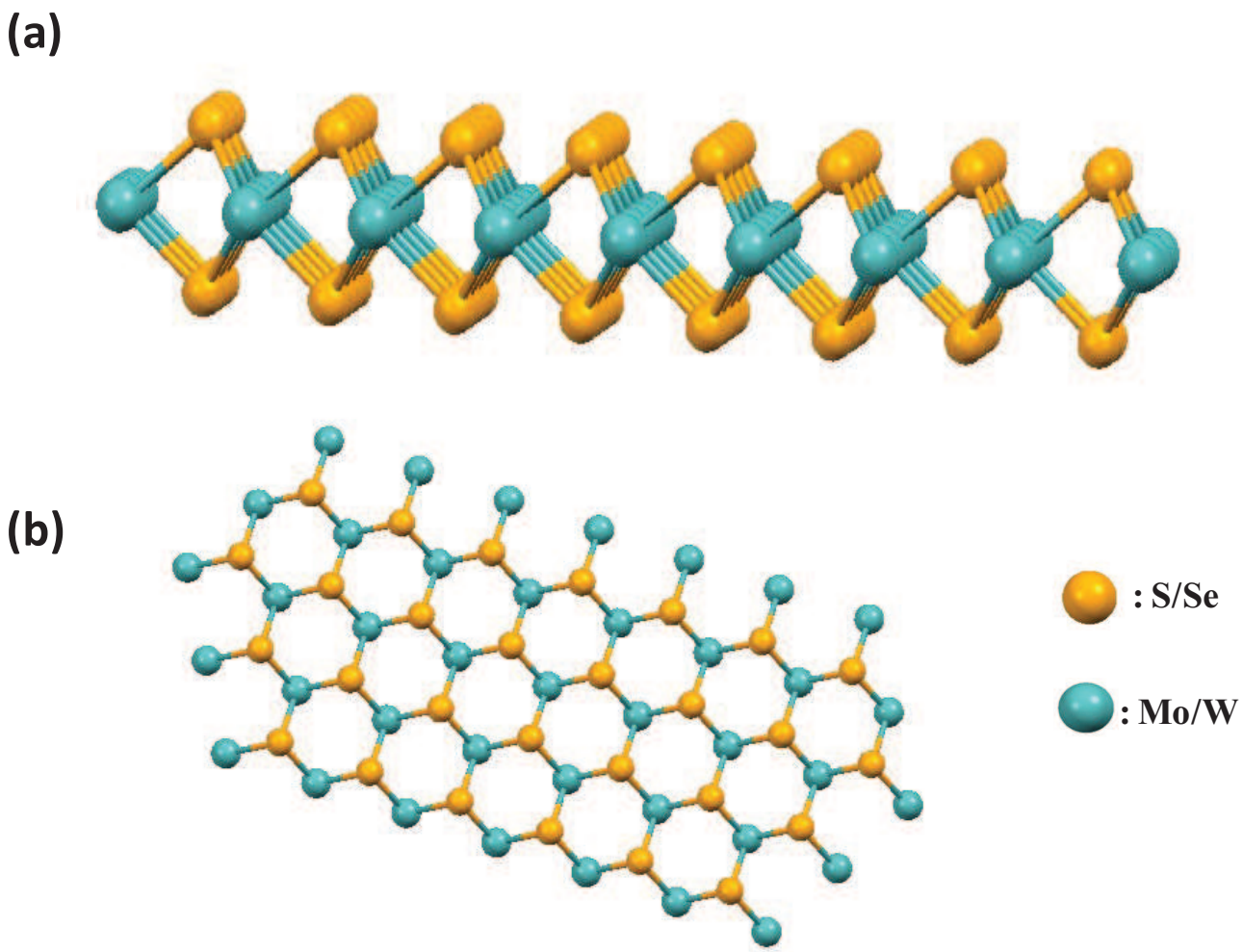

Figure S2: Three dimensional Representations of single layer TMDCs (a) side view (b) top view.

Figure S3:

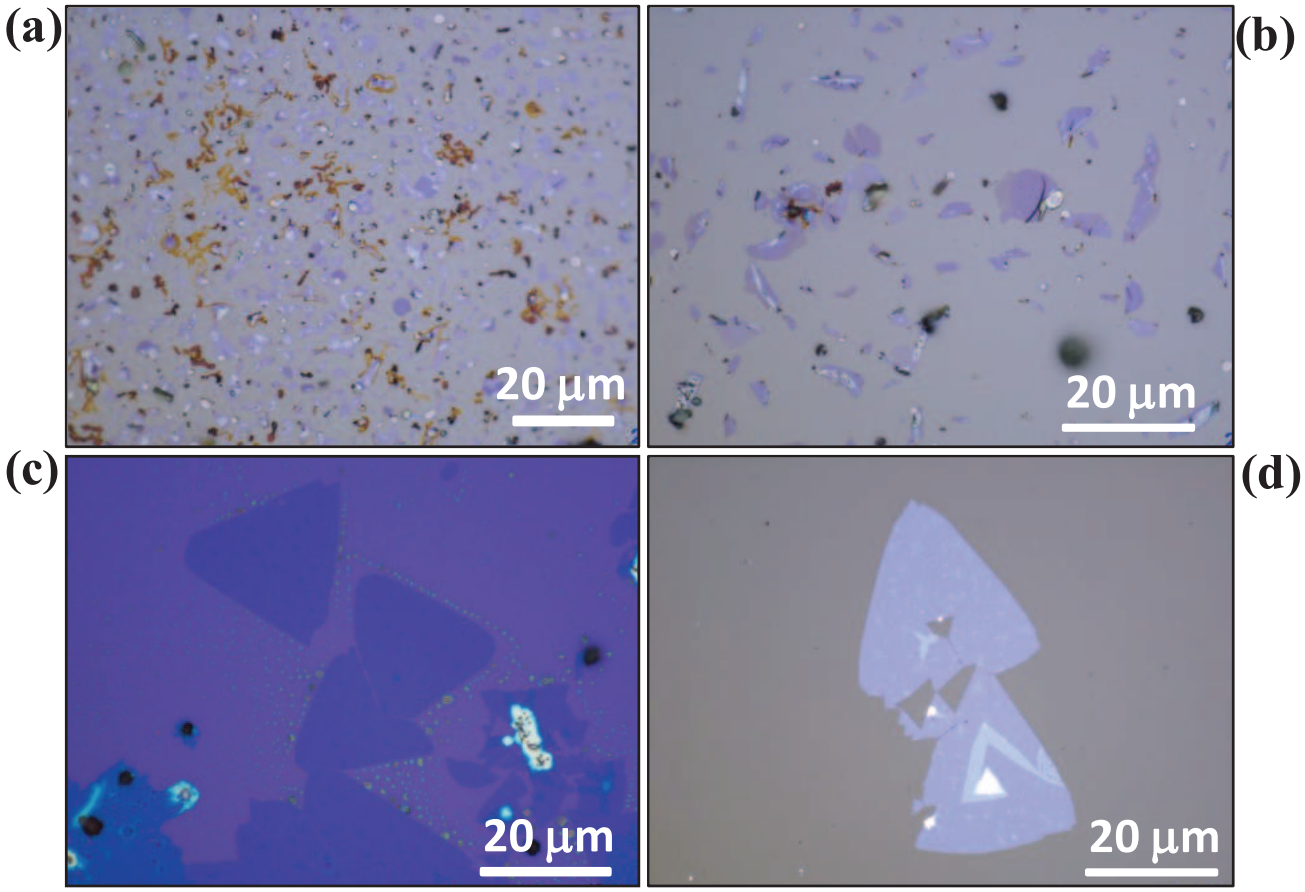

Figure S3: Optical image for CVD grown MoS_2 monolayer sample on various substrate (a) *n*-Si (b) *p*-Si (c) SiO_2/Si and (d) quartz.

Figure S4:

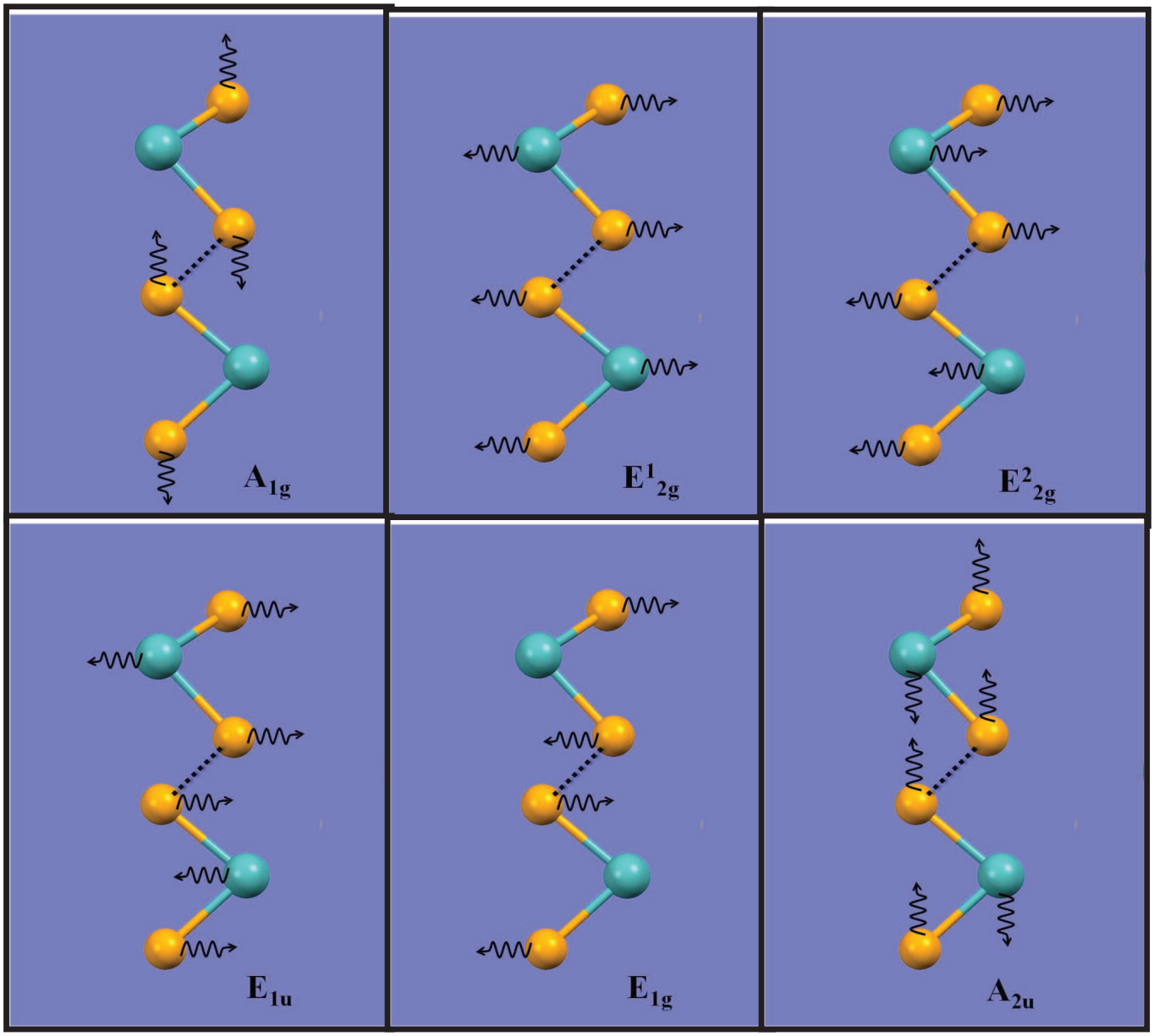

Figure S4: Possible vibrational modes (A_{1g}, E^1_{2g}, E^2_{2g}, E_{1u}, E_{1g} and A_{2u}) for transition metal dichalcogenides.

Figure S5:

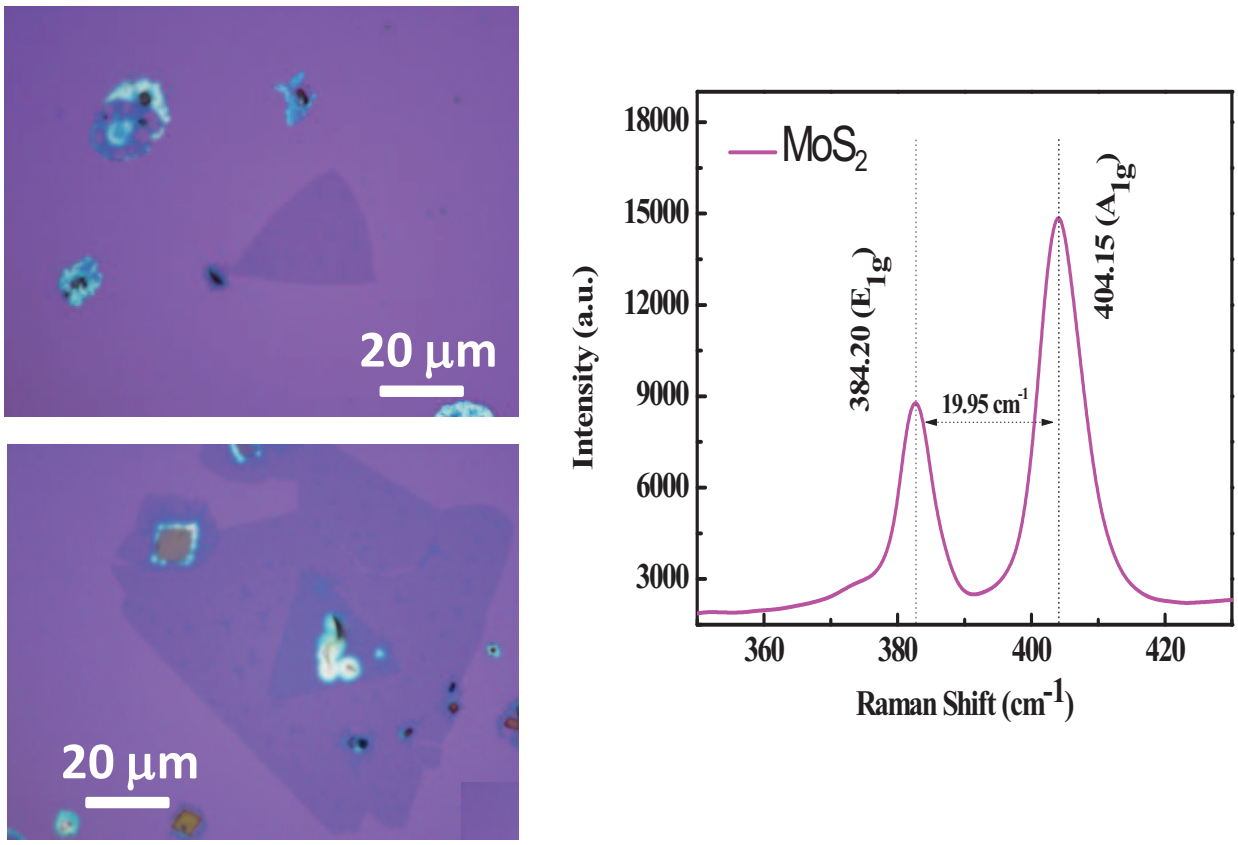

Figure S5: Typical optical microscope image and Raman spectra of large area CVD grown monolayer MoS_2.

Figure S6:

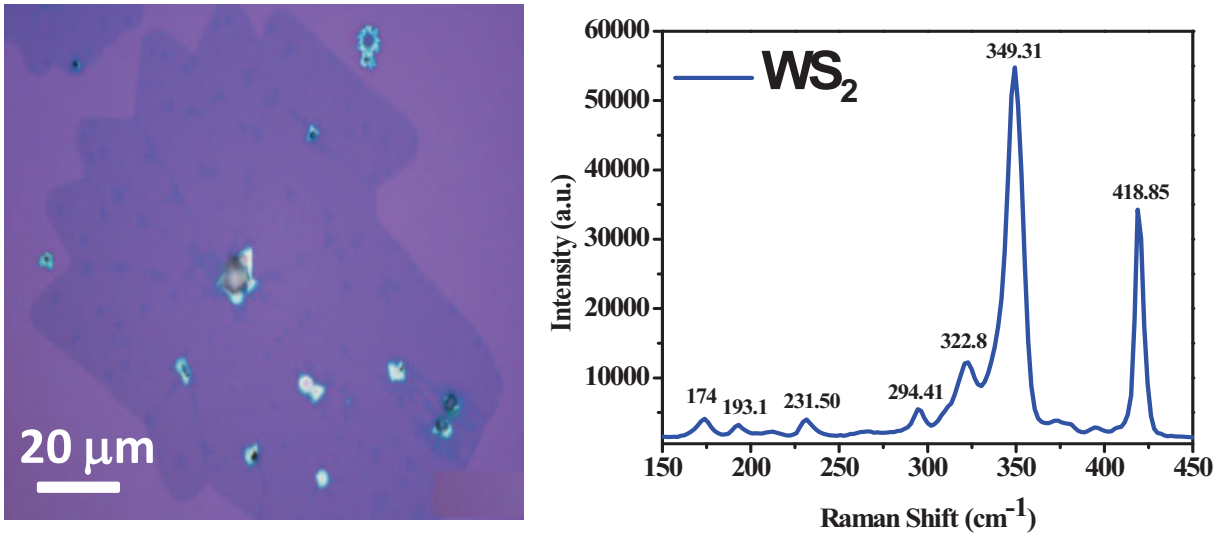

Figure S6: Typical optical microscope image and Raman spectra of large area CVD grown monolayer WS_2.

Figure S7:

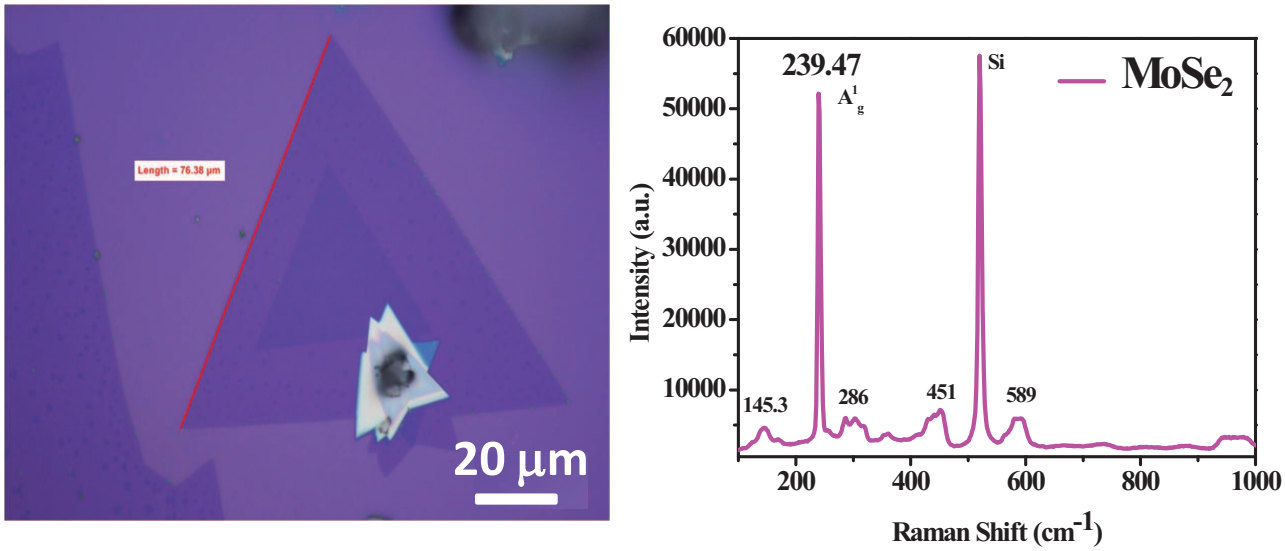

Figure S7: Typical optical microscope image and Raman spectra of large area CVD grown monolayer $MoSe_2$.

Figure S8:

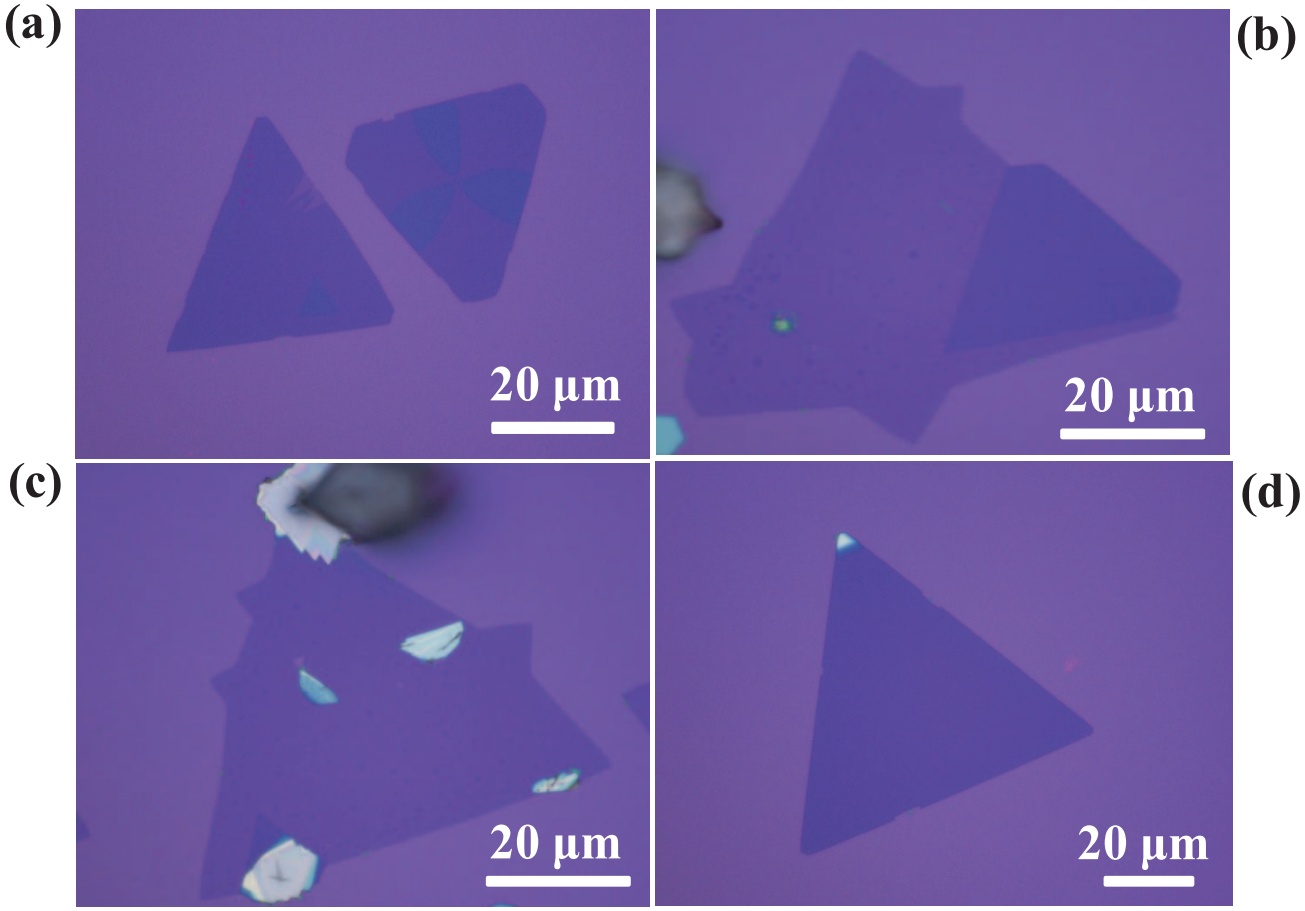

Figure S8 (a-d): Typical optical images for CVD grown $MoSe_2$ nanosheets.